Mechanisms of skin vascular maturation and maintenance captured by longitudinal imaging of live mice

Chen Yuan Kam[1], **Ishani D. Singh**[1], **David G. Gonzalez**[1], **Catherine Matte-Martone**[1], **Paloma Solá**[#,2], **Guiomar Solanas**[#,2], **Júlia Bonjoch**[2], **Edward Marsh**[1], **Karen K. Hirschi**[*,3], **Valentina Greco**[*,1,4,5]

[1]Department of Genetics, Yale School of Medicine, New Haven, CT 06510, USA

[2]Institute for Research in Biomedicine (IRB Barcelona), The Barcelona Institute of Science and Technology, 08028 Barcelona, Spain.

[3]Department of Cell Biology, University of Virginia School of Medicine, Charlottesville, VA 22908, USA.

[4]Departments of Cell Biology and Dermatology, Yale Stem Cell Center, Yale Cancer Center, Yale School of Medicine, New Haven, CT 06510, USA

[5]Lead author

SUMMARY

A functional network of blood vessels is essential for organ growth and homeostasis. Yet, how the vasculature matures and maintains homeostasis remains elusive in live mice. By longitudinally tracking the same neonatal endothelial cells (ECs) over days to weeks, we found that capillary plexus expansion is driven by vessel regression to optimize network perfusion. Neonatal ECs rearrange positions to evenly distribute throughout the developing plexus and become positionally stable in adulthood. Upon local ablation, adult ECs survive through a plasmalemmal self-repair response while neonatal ECs are predisposed to die. Furthermore, adult ECs reactivate migration to assist vessel repair. Global ablation reveals coordinated maintenance of the adult vascular architecture that allows for eventual network recovery. Lastly, neonatal remodeling and adult maintenance of the skin vascular plexus are orchestrated by temporally restricted, neonatal VEGFR2 signaling. Our work sheds light on fundamental mechanisms that underlie both vascular maturation and adult homeostasis *in vivo*.

[*]Co-correspondence to: Valentina Greco, valentina.greco@yale.edu, Karen K. Hirschi, kkh4yy@virginia.edu.
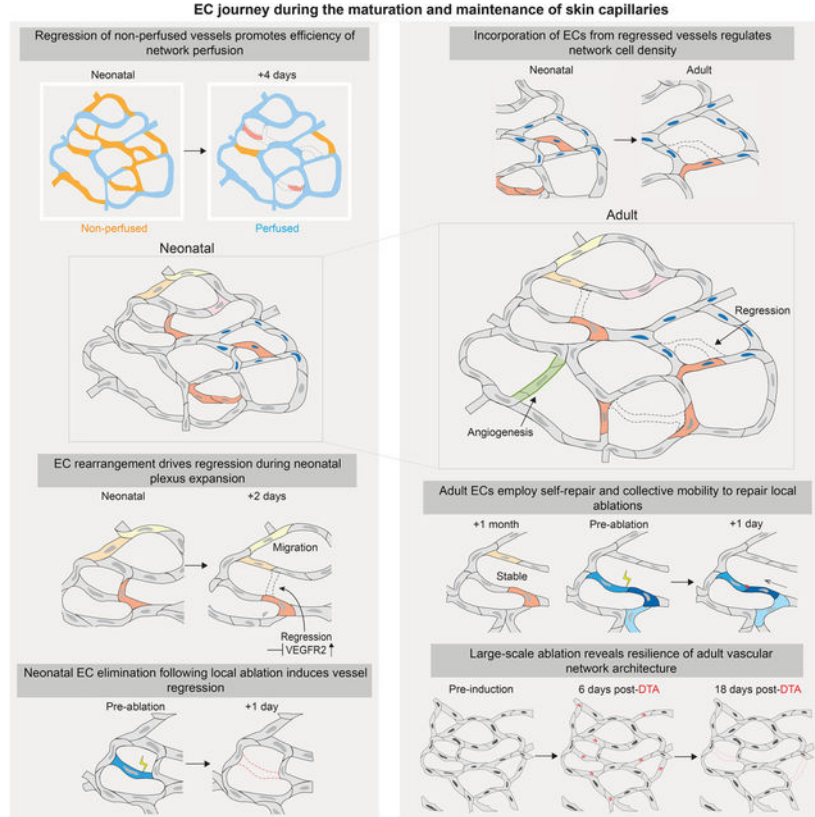[#]These authors contributed equally

DECLARATION OF INTERESTS

The authors declare no competing financial interests.

Graphical Abstract

EC journey during the maturation and maintenance of skin capillaries

IN BRIEF

Maturation and expansion of skin vasculature is driven by vessel regression with endothelial cells rearranging to distribute and optimize network perfusion. During adulthood, positionally stable cells reactivate migration to assist vessel repair. Following membrane injury, adult endothelial cells survive through a self-repair response, while neonatal cells are predisposed to die leading to vessel regression.

INTRODUCTION

Proper organ function requires an optimally constructed vascular network to ensure an adequate supply of nutrients and soluble factors via the bloodstream[1]. This ability is particularly relevant to capillaries, the small diameter vessels that function as the primary conduits for transport of soluble factors, nutrients, and immune cells to perfused tissues[2–4]. Endothelial cells (ECs) are the functional units of capillaries, consisting of specialized squamous cells that form the inner lining of all blood vessels[5]. ECs execute many processes involved in vascular network formation, refinement, and function by regulating fundamental aspects of vessel morphogenesis[5–10].

The period immediately following birth is known as the neonatal developmental stage. It is an understudied, critical window that bridges the morphogenic events of embryogenesis

to adult homeostasis[11–15]. Yet, there are significant gaps in our understanding of the tissue, cellular and molecular mechanisms involved in postnatal vessel network maturation and maintenance of adult vascular homeostasis. This is largely due to technical challenges associated with long-term tracking of changes in vascular architecture, function, and underlying EC behaviors, particularly within mammalian model systems. The skin functions as an essential barrier to the external environment[16,17]. Skin capillaries play a vital role in maintaining organ homeostasis: they control body temperature, regulate immune surveillance, and transport nutrients and paracrine factors[18–20].

Here, we investigated cellular-, tissue-, and molecular-level mechanisms that define the maturation, maintenance, and function of the mouse skin capillary plexus via our longitudinal intravital imaging approach[21]. We found that capillary plexus maturation is mediated by coordinated regression and rearrangement of existing ECs to optimize network perfusion. Adult ECs become positionally stable but maintain vessel and network integrity via coordinated behaviors of neighbors. Furthermore, adult but not neonatal ECs preferentially survive damage through a plasmalemmal self-repair mechanism that prevents vessel regression. Collectively, our work demonstrates that distinct mechanisms regulate postnatal skin maturation and vascular homeostasis in adult skin, and that responses to cellular loss differ in the context of scale and developmental stage.

RESULTS

Vessel regression drives maturation of the capillary network to optimize network perfusion

The mouse skin vasculature resides in the dermis and is organized in connected plexuses throughout the organ (Figures S1A–C). We sought to elucidate the mechanism by which the skin superficial capillary plexus matures into an adult network. To achieve this, we focused on the neonatal developmental period and visualized blood vessels in live mice[21]. We conducted our studies in palmoplantar skin as this anatomical region offers a simplified model devoid of cycling appendages[22,23].

To label the vascular architecture, we utilized an EC restricted Cre driver, recombining membrane-GFP specifically in ECs *(VECadCreER; mTmG)*[24,25] (Figures 1A–1B). We compared the skin capillary plexus as it expands during various postnatal periods, including neonatal mice at postnatal day 5 (P5), weanling (P21), and juvenile (P35) stages. P5 mice exhibited significantly smaller capillary loops and more abundant branching points compared to P21 cohorts (Figures 1A, 1A' and 1A"). In addition, we observed an overall decrease in vascular coverage in the older mice (Figures 1A and 1A'''). When comparing P21 and P35 mice, these differences were not observed, indicating that the majority of postnatal vascular remodeling occurs before weaning (P21).

We next investigated the mechanisms responsible for the observed changes in vascular architecture by longitudinally tracking these same vessels over time. We revisited the capillary plexus at P5-P9-P15 and identified active remodeling events such as vessel regression (Figure 1C; Red inset) and new vessel growth (angiogenesis) during this time period (Figure 1C; Green inset). Quantifications of these events over larger areas (>300,000 μm^2) during P5-P15 show that vessel regression significantly outpaced angiogenesis at both

the P5-P9 (4:1 ratio) and P9-P15 (18:1 ratio) intervals (Figure 1C'). Furthermore, these rates were comparable between hairy and non-hairy skin (Figures S1D–S1E).

In accordance with previous studies[26], vessels undergoing regression were indistinguishable from those undergoing angiogenesis as ~70% of vessel "sprouts" tracked from P5 to P9 resulted in regression (Figures S2A–S2A'). Similarly, lateral filopodia, established indicators of remodeling vessels, significantly decreased as the network matured (Figures S2B–S2B')[27]. To characterize the kinetics of vessel regression, we performed daily revisits and found that while some segments regressed within 1–2 days (Figure S2C), others took up to 4-days to completely regress (Figure S2D). Intriguingly, many angiogenesis events from P5-P9 were transient as ~70% of these segments were found to be regressed at P15 (Figures 1D–1D'). In contrast, newly formed vessels in a wound context were largely maintained (>80%) (Figures S2E–S2E'), indicating that transient angiogenesis may be a feature of developing vessel beds.

Hemodynamics are critical in the regulation of vascular remodeling[7,28,29]. To investigate the functional relationship between vessel regression and blood flow, we visualized red blood cells (RBCs) via third harmonic generation (3HG) imaging (Movie S1)[30]. Intriguingly, a substantial proportion (~50%) of capillaries were non-perfused during neonatal stages, whereby non-perfused vessels displayed either a lack of 3HG signal or the presence of stalled RBCs (Figures 1E–1E'). As we tracked these vessels, we found that the percentage of non-perfused vessels was reduced over neonatal development (Figures 1E–1E'). Furthermore, the majority of vessels fated for regression (~90%) were non-perfused (Figures 1E and 1E"), though lack of perfusion was not a guarantee for subsequent regression. Poor network perfusion may influence the hypoxic status of the skin, which was found to be significantly higher at P5 compared to P21 as assessed by pimonidazole-HCl labeling (Figures S2F–S2F'). Collectively, our findings build upon principles of network optimization observed in other model systems[28] and suggest that the vessel remodeling program of the dermal capillary plexus is driven by network-wide regression leading to optimization of network perfusion.

Neonatal ECs participate in plexus-wide positional rearrangement and execute vessel regression via migration.

We next sought to understand the cellular mechanisms underlying vessel regression. We visualized single ECs via a minimal dose of tamoxifen administered to *VECadCreER; mTmG* mice (Figure 2A). We performed longitudinal imaging of single-labeled ECs over the postnatal period spanning P5-P15 and specifically monitored the fate of ECs in vessel segments that ultimately underwent regression. We successfully identified the same cells at successive time points in nearly all regression events (37/38), indicating that EC apoptosis is not a significant contributor to vessel regression. Instead, we found that ECs migrated from regressing segments into adjacent vessels (Figures 2A–2A'). Similar regression mechanisms have been described in zebrafish brain and mouse retinal vascular development[26,28,31], pointing to migration-mediated regression as a conserved developmental mechanism in vascular biology.

Most strikingly, we found that EC migration was broadly distributed and not restricted to regressing segments; indeed, we found evidence of EC migration in non-remodeling vessels (Figure 2B). As they changed positions, these ECs adapted their cellular morphology to the plexus structure, migrating within the endothelial layer. Analysis of EC migration (Figure S3A) over the P5-P11 interval revealed that the average rate of EC migration decreases over developmental time (Figure 2B'). We also employed an independent strategy based on the use of an EC nuclear reporter (*VECadtTA; pTREH2BGFP; mTmG*) allowing for simultaneous tracking of all ECs (Figure 2C)[32,33]. Overlay of a conserved capillary loop at P5 and P7 revealed minimal positional overlap of EC nuclei, confirming that the vast majority of capillary ECs undergo positional rearrangement (Figures 2C–2C'). The direction of EC migration was largely polarized against the direction of blood flow, consistent with other model systems (Figures 2D, 2D' and S3B)[7,10,34]. These EC migratory behaviors were also found in larger caliber venules and arterioles of the dermal microvasculature (Figure S3C). The migration rates of venule and arteriole ECs were both consistent with the migration rates observed in capillaries (<100 μm over 4 days) (Figure S3C'). Our findings show that skin capillaries execute selective vessel regression through a migratory mechanism and that ECs undergo network-wide migration and rearrangement that decrease throughout neonatal development.

Cellular density in the developing plexus is locally controlled by the incorporation of ECs from regressed segments.

The widespread movement of ECs during skin development suggests that local cell density might be affected as cells from regressing segments are incorporated into nearby capillary loops. We hypothesized that capillary loops containing regressed segments would exhibit a larger increase in cell number than conserved loops without regressions. To test this, we determined the net change in EC number by tracking "conserved loops" and "regression-containing loops" from P5 to P21 (Figure 3A). Interestingly, not accounting for P5 ECs fated for regression (white asterisks), by excluding them from the analysis, showed that regression-containing loops displayed a significant increase in the change of cell number compared to conserved loops (Figures 3A, 3A' and S4C). However, when regressed ECs were included in the P5 cell counts, there was no longer a significant difference in the net change of EC number between conserved loops and regression-containing loops, indicating that regressed ECs were incorporated into the P21 capillary loops (Figure 3A"). We next investigated whether EC proliferation or apoptosis contributed to the regulation of EC density in the remodeling plexus. Phospho-Histone H3 (pHH3) immunostaining showed that active EC proliferation is very low (<0.4%) at P5 (Figures S4A–S4A'). We further probed EC proliferation via daily injections of EdU from P5-P8 and found that ~4% of ECs are EdU positive within this time window (Figures S4B–S4B'). Altogether these data show that EC proliferation does not appear to be a major contributor to plexus expansion. Furthermore, when surveying EC nuclei morphology in neonates, we did not detect apoptotic bodies, a method we have previously used to score apoptosis events reliably (data not shown)[35].

We next investigated plexus-wide changes in EC density by analyzing large numbers of ECs (>500 cells) during plexus expansion from P5 to P21 (Figure 3B). Interestingly, when controlling for conserved area, EC density was reduced by ~2-fold in P21 compared to

P5 mice (Figure 3B'). However, EC density was largely maintained when assessed relative to the original, architecturally conserved vessel structures (Figure 3B"). Assessment of EC internuclear distance between P5 and P21 vessels revealed a significant increase of internuclear distance in P21 compared to P5 vessels (Figure S4D), suggesting that EC expansion may also contribute to loop expansion.

Lastly, given that our analysis of plexus expansion was performed within the XY-plane, we sought to determine if similar principles of network expansion applied to the XZ-axis. To our surprise, we did not detect appreciable expansion of this network in the XZ-plane and instead the same vessel structures were found at corresponding depths across revisits (Figure S5 and Movie S2). Together, our results demonstrate that EC density in the remodeling plexus is regulated by the incorporation of ECs from regressed vessels, allowing for the expansion of the capillary network during postnatal development.

ECs become positionally stable in adulthood but coordinate neighborhood rearrangement in response to local ablation.

The decreasing rate of EC migration during neonatal development prompted us to investigate whether ECs continue to change positions in the adult plexus. To answer this question, we labeled ECs at P35 and revisited the animals 1-month later at P63. We detected negligible amounts of displacement over this 1-month interval (Figures 4A–4A'). The observed cessation of cellular mobility parallels the lack of vessel remodeling observed in adult vessels.

Considering the stability of the adult plexus, we next sought to determine how vessel maintenance is achieved following neighboring cell loss. To address this, we performed localized ablation using the two-photon laser. These ablations were directed at sites adjacent to single labeled ECs, allowing for assessment of nearby responses when revisited 1-day later (Figure 4B). Interestingly, we found that neighboring ECs responded to ablation by either reactivating migration or elongating towards the ablation site (Figures 4B–4C). Quantification of the cumulative responses of ablation-adjacent ECs showed that >90% of the labeled cells responded by either elongating or migrating towards the ablation site with equal probability (Figures 4B'–4B").

To assess the extent of neighbor participation following ablation, we employed models to label more than just one cell. By marking two flanking ECs, we show a rapid response of both cells elongating towards the ablation site and closing the distance between each other by 24-hour revisit (Figure 4C and Movie S3). By marking all nuclei, we show that EC positional rearrangement occurred primarily within the afflicted segment at 24-hours post-ablation, along with further positional adjustments within neighboring segments 1-week post ablation (Figure 4D). No proliferation or EC replacement were captured. Collectively, these data demonstrate that adult ECs are positionally stable under homeostatic conditions. Following local ablation, these cells do not proliferate but rather mount a coordinated rearrangement response that effectively repairs the afflicted vessel.

Network-wide ablation of adult ECs reveals the coordinated maintenance of plexus architecture by surviving ECs.

The robustness of vessel architecture preservation in the face of limited cellular loss prompted us to investigate the response of the adult network to large-scale ablation of ECs. To test this, we utilized *VECadCreER; R26DTA* animals that express diphtheria toxin (DTA) specifically in ECs upon tamoxifen administration[36], combined with *VECad-mTnG* animals that express constitutive nuclear (H2B-GFP) and membrane (tdTomato) in ECs[37] (Figure 5A). Administration of 200 µg of tamoxifen led to induction of EC death throughout the vasculature while preserving the survival of the animal (Figure 5A). Ablation of ~25% of adult ECs by 6-days post-induction (D6) (Figures 5B–5B'), induced regression of only ~5% of vessels compared to pre-induction (D0) (Figure 5B"), indicative of significant compensation from the remaining network ECs. This was highlighted by various instances whereby small numbers of ECs (1–2) were able to maintain vessel connections by extending their cell bodies (Figure 5C). We hypothesized that vessel segments subject to a higher number of EC losses at D6 would be more susceptible to induced regression. However, quantification of the change in EC number/vessel length from D0 to D6 in maintained versus regressed segments showed no statistical difference (Figures 5D–5D'). Rather, we detected a significant difference between the EC number/vessel length at D0 in maintained versus regressed segments (Figures 5D and 5D"), suggesting that segments with a higher starting number of ECs are better able to withstand cellular losses and avoid induced regression.

Further tracking of EC density at D12 and D18 showed a partial recovery of overall EC density (Figure 5B'), consistent with proliferative response of network ECs following large-scale injury shown previously[8,38]. However, this recovery (D6 vs D18) was not statistically significant, likely due to the permanent elimination of vessel segments lost to regression. A closer inspection of vessels that were maintained following DTA ablation confirmed this as we found a significant recovery of ECs/vessel length from D6 to D18 in maintained segments (Figures 5D and 5D"). Furthermore, even within maintained vessels, we still observed a significant difference between the ECs/vessel length in D0 compared to D18 conditions (Figure 5D"). These results indicate that while the adult network is able to recover in response to plexus-wide losses, this recovery falls short of the original state of the plexus from both the standpoint of plexus architecture and network density distribution. Collectively, these data demonstrate the resilience of the adult EC network architecture that is mediated by the coordinated behaviors of surviving ECs in response to large-scale cellular loss.

Adult but not neonatal ECs preferentially activate a plasmalemmal self-repair mechanism to survive membrane damage and preserve vessel architecture.

To better understand the repair process following local ablation, we next interrogated the mechanism by which damaged ECs are cleared while maintaining the structural integrity of the vessels. We visualized the spatiotemporal dynamics of EC death and clearance following targeted laser ablation using time-lapse microscopy. Remarkably, we found that many adult ECs did not die; instead, they survived by excising portions of their cell body upstream of the damage site within the first hour following ablation (Figure 6A and Movie S4). This response was followed by EC elongation towards the ablation location. We next determined

the fate of injured adult ECs 24-hours following laser ablation (Figure 6B; top panel). We found that the majority of membrane-damaged adult ECs (>60%) were present 24-hours following laser ablation (Figures 6B–6B'). In contrast, only ~20% of neonatal (*i.e.*, P5-P7) ECs were maintained 24-hours post-ablation (Figures 6B–6B'). These observations show that plasmalemmal self-repair is utilized by adult ECs to a much greater extent (*i.e.*, 3-fold) compared to neonatal ECs.

To further understand EC death or survival at different developmental stages, we performed time-lapse imaging of neonatal ECs following laser ablation. Interestingly, neonatal ECs exhibited rapid whole-cell membrane blebbing as the cell died (Figure 6D and Movie S6). In contrast, adult ECs that underwent cell death did not exhibit peripheral membrane blebbing but rather a gradual clearance of the labeled cell (Figure S6). Surviving adult ECs also exhibited membrane blebbing close to the ablation site in addition to the excision mediated mechanism observed (Figures 6A, 6C, Movie S4 and Movie S5).

To probe the functional consequence of these ablations, we monitored blood flow in response to ablations. We found that 1-hour post-ablation, blood flow was halted specifically in the afflicted segment (Figure 6E). Revisiting 24-hours later showed a recovery of blood flow within the ablated segment (Figure 6E) demonstrating that temporary cessation of flow occurs while ECs carry out coordinated behaviors to repair the injured vessel.

The observed differences in cell survival following ablation in neonatal compared to adult ECs prompted us to investigate the implications at the tissue level. We assessed the fate of vessel segments and showed that *all* adult vessels evaluated were maintained 24-hours post-ablation (Figures 6F–6F'). In contrast, neonatal vessels were maintained in only ~30% of the vessels tracked; most neonatal vessels underwent regression following laser ablation (Figures 6F–6F'). Together, our findings point at an age-dependent divergence in the regulation of EC membrane repair in response to local ablation.

Neonatal vessel regression, optimization of network perfusion, and adult maintenance are orchestrated by neonatal VEGFR2 signaling.

To understand the molecular underpinnings of vascular maturation, we turned to a critical vascular signaling pathway- VEGF-A signaling[39]. We first assessed the expression of VEGF-A and its cognate receptor VEGFR2 during postnatal skin development. We determined that VEGF-A expression was significantly higher (~3-fold) in P6 skin compared to P15, a difference that was not observed in P15 versus adult skin as assessed by ELISA (Figure 7A). Whole-mount immunostaining for VEGFR2 showed enriched expression in blood vessels at P5, in contrast to broad dermal expression at P21 (Figure 7B). Furthermore, FACS analysis of VEGFR2 expression on ECs reveals a mild but significantly lower expression of VEGFR2 at P21 compared to P5 (Figures S7A–S7B'). Altogether, analyses of ligand and receptor protein expression suggest that VEGF-A signaling via VEGFR2 may play a regulatory role during the skin vascular maturation process.

To test whether VEGFR2 signaling plays a role towards skin vascular maturation, we employed DC101, a potent and specific inhibitor of VEGFR2[40,41] (Figures S7C–S7C''). Tracking of treated mice (injected at P4 and P7) from P5 to P9 (Figure 7C) showed that

DC101-treated animals displayed ~2-fold higher levels of vessel regression in the P5-P9 interval when compared to vehicle-treated littermates (Figure 7D–7D'), consistent with a previous study that utilized genetic deletion of VEGFR2[42].

Further tracking at P21 showed overall healthy plexus morphology and vessel coverage in both conditions (Figure S7D–S7D'), suggesting that DC101 led to an acceleration of the physiological vessel remodeling program. To understand the functional consequences of this accelerated remodeling, we performed network blood flow analysis at P9. We found that DC101-treated mice displayed a significantly higher percentage of perfused vessels compared to controls (Figures 7E–7E'). This result shows that VEGFR2 regulated acceleration of vessel regression results in a corresponding acceleration of network perfusion.

Lastly, to understand the longer-term consequences of neonatal VEGFR2 blockade, we continued to track these mice into adulthood at 2-months of age. Intriguingly, when compared to vehicle-treated controls, DC101-treated animals displayed abnormal vessel morphology, with widespread distribution of vessel kinks and tortuous capillaries, established indicators of unhealthy or diseased vessels (Figures 7F–7F')[9,43–45]. Furthermore, this morphology was reminiscent of vessel structures that we had previously observed in control 6-month old animals (Figure 7F). These results show that blockade of vascular VEGFR2 signaling during neonatal stages leads to premature deterioration of vessel structure and more aged morphology. These findings emphasize the importance of the vascular maturation process and how dysregulation of VEGF-A/VEGFR2 signaling during this critical window can lead to impaired vascular homeostasis in adulthood.

DISCUSSION

This study shows that neonatal vessel remodeling in the expanding plexus is driven primarily by network-wide vessel regression that favors the elimination of non-flowing vessels to optimize network perfusion. The majority of new vessels formed via angiogenesis represent transient connections fated for regression. These findings indicate that neonatal remodeling of skin capillaries favors an overall reduction in vessel coverage and raises several questions regarding the purpose and regulation of these transient vessel connections. It was previously proposed that external signals promote the formation of new vessels fated for elimination as a strategy to favor regression of immature vessel segments[46]. Alternatively, these vascular structures may play functional roles in the stereotyped remodeling of the developing plexus. Future studies should focus on elucidating the regulation of transient vessel formation as this process may have important implications for angiogenic remodeling in other developmental systems or pathological states.

We find that plexus-wide rearrangement and incorporation of ECs from regressed vessels serves as a mechanism to regulate EC density in the growing plexus. It is well established that ECs adopt cellular quiescence in adulthood and actively repress their proliferative capacity under homeostatic conditions[47,48]. Our findings suggest that the suppression of EC proliferation begins early in postnatal life, as the capillary plexus favors the reabsorption of regressed ECs and increases in EC size over increasing EC number as a mechanism for

plexus expansion. These results shed light upon shared and divergent cellular mechanisms that underlie vessel regression in developmental versus pathological states[46,49–51].

Establishing the positional and architectural stability of ECs during adulthood allowed us to investigate the cellular mechanisms utilized by ECs to maintain homeostasis. We observed that capillary ECs do not proliferate in response to local ablations but rather compensate for the loss of neighbors through membrane remodeling. Network-wide EC ablation revealed that large losses of ECs (~25%) led to limited induction vessel regression and subsequent partial recovery of EC numbers. This finding has important implications for various cardiovascular, immune and inflammatory diseases that are known to cause wide-spread EC apoptosis as it suggests a permanence of the damage inflicted to an endothelial network. Overall, these results provide valuable knowledge towards the differing cellular mechanisms employed by EC networks to mediate the repair and recovery towards small scale injuries that resemble homeostatic loss of ECs due to wear and tear versus the wide-scale EC apoptosis that is characteristic of various pathologies.

In addition to neighboring EC responses, we uncovered a divergence of fates in neonatal versus adult ECs following local membrane ablation. The ability of adult ECs to self-repair is reminiscent of the membrane resealing capacity observed in muscle fibers, an ability believed to have evolved owing to the frequency of membrane injuries resulting from repeated muscle contraction[52,53]. Considering the persistent exposure of ECs to shear and contractile forces associated with blood flow, it is plausible that ECs evolved similar capacities for self-repair as a protective measure against injuries related to these forces.

In summary, our work describes the postnatal journey of ECs and their role in the maturation and maintenance of the capillary network. It establishes an understanding of the cellular mechanisms that dictate neonatal vascular development and adult homeostasis. Our findings lay the foundation for understanding of pathologies and conditions characterized by vessel rarefaction or impaired vascular maintenance, such as scleroderma, primary hypertension, and aging[49–51]. Furthermore, our results contribute to a deeper understanding of therapeutics that facilitate vessel maturation such as those that target the VEGF signaling pathway, as well as improve drug delivery during tumorigenesis[54].

Limitations of the study

In this study, we focused on understanding the developmental remodeling and maintenance of the skin microvascular network, with particular emphasis on capillaries. Future studies should focus upon understanding the conserved and diverging principles of our findings within veins and arteries. Another potential consideration is our use of pan-endothelial drivers (VE-Cadherin promoter) that do not account for possible heterogeneity within subpopulations of ECs. Subsequent studies that employ single cell RNA sequencing approaches to identify potential markers of specialized ECs during development and repair would be exciting directions that improve our resolution of these fundamental processes while providing potential targets for therapeutics.

STAR METHODS

RESOURCE AVAILABILITY

Lead Contact—Further information and requests for resources and reagents should be directed to and will be fulfilled by the Lead Contact, Valentina Greco (valentina.greco@yale.edu).

Materials Availability—This study did not generate new unique reagents.

Data and Code Availability

- All original data are available upon reasonable request to Lead Contact.

- This paper does not report original code.

- Any additional information required to reanalyze the data reported in this paper is available from the Lead Contact upon request.

Experimental Model and Subject Details

Mice: *VE-CadherinCreER* (*VECadCreER*)[24] and *VECadherin-mTnG (VECad-mTnG)*[37] *mice* were obtained from Ralf Adams (Max Planck Institute). Elaine Fuchs (Rockefeller University) provided *pTRE-H2BGFP* mice[33]. *Rosa26-loxP-membraneTomato-(stop)-membraneEGFP (mTmG)*[25] *VE-CadherintTA* (*VECadtTA*)[32], and *R26-LSL-DTA*[36] mouse lines were from The Jackson Laboratory. All mice were bred to a mixed CD1 albino background. The animals used in this study were of both genders and within an age range of P1 to P21 for postnatal development studies and 2–4 months for adult studies. The experiments were not randomized. The investigators were not blinded to allocation during experiments and outcome assessment. All experimentation involving animal subjects was approved by the Institutional Animal Care and Use Committee at Yale School of Medicine and conducted following the approved animal handling protocol.

Method Details

In vivo imaging: In vivo imaging procedures were carried out as previously described[21]. Mice were anesthetized in an isoflurane chamber and continuously received vaporized isoflurane through a nose cone (1% oxygen and air) on a warm heating pad for the duration of the analysis. A LaVision TriM Scope II (LaVision Biotec) laser scanning microscope equipped with a Chameleon Vision II (Coherent) two-photon laser (using 940 nm for live imaging and whole-mounts) and a Chameleon Discovery (Coherent) two-photon laser (using 1120 nm for live imaging and whole-mounts) was used to acquire z-stacks of 100–200 μm in 1–2 μm steps through either a Nikon 25×/1.0 or a Nikon 40x/1.15 water immersion objective. Optical sections were scanned with a field of view of 0.44×0.44 mm^2 or 0.28×0.28 mm^2, respectively, at 700 Hz. To visualize large areas, we imaged 4–24 tiles of optical fields with a motorized stage and automatically acquired sequential fields of view, as previously described. For time-lapse imaging, serial optical sections were obtained in a range of 5–20 min intervals, dependent upon experimental setup with a duration of 1–5 hours. For imaging of blood flow via third harmonic generation (3HG), the Chameleon Discovery (Coherent) two-photon laser was tuned to 1275 nm, allowing for label-free

detection of red blood cells. To evaluate network perfusion status, 3HG imaging at fine Z-increments (0.5 μm) whereby repeated scanning through vessel lumens when projected maximally provided a visualization of vessel perfusion status.

Tamoxifen induction: To induce maximal expression of membrane-GFP labeling in neonates, *VECadherin-CreER; mTmG* mice received intragastric injections of 100 μg of tamoxifen at postnatal days 1 (P1) and P2. To induce single cell labeling in neonates, mice received intragastric injection of 2 μg of tamoxifen at P2. To induce single cell labeling in adults, mice received intraperitoneal injection of 10 μg of tamoxifen at least 3-days prior to imaging. To induce dipththeria toxin (DTA) expression, *VECadherinCreER; R26-LSL-DTA; VECadherin-mTnG* adult animals were administered with 200 μg of tamoxifen via intraperitoneal injection prior to *in vivo* imaging at indicated time-points. Tamoxifen (Sigma) stocks were prepared by dissolving 200 mg of tamoxifen powder in 10 mL of corn oil. 2 mg aliquots were stored at –20°C and diluted in the required volume of corn oil before injection.

VEGFR2 neutralization: Inhibition of VEGFR2 was carried out by intraperitoneal injection of an anti-VEGFR2 neutralizing antibody (DC101, BioXcell) at a concentration of 20 mg/kg in PBS or vehicle (PBS) alone as a control. DC101 or vehicle treatment was carried out at P4 and P7.

Wound induced angiogenesis: Mice were anesthetized by intraperitoneal injection of ketamine and xylazine cocktail mix (100 mg/kg and 10 mg/kg, respectively in phosphate-buffered saline). Once a surgical plane of anesthesia was verified by the absence of a physical and physiologic response to a noxious stimulus, a punch biopsy was performed using a 1 mm diameter punch biopsy tool (Miltex, USA). The punch biopsy tool was used to make a circular full thickness wound on the palmoplantar side of the mouse hind paw.

Laser ablations: Laser ablations were carried out using a Chameleon Vision II (Coherent) two-photon laser at a wavelength of 810 nm, using either a Nikon 25×/1.0 or Nikon 40×/1.15 water immersion objective with 10% laser power. Experimentally, the field of view of the scanning head was reduced to a 1 μm² sized window and positioned at the location to be ablated. We then activated the "live" scan function until a mild autofluorescence signal became visible in the green channel (~3–5 seconds). For adjacent ablation experiments, ablations were positioned ~30 μm away from a labeled EC. For experiments involving ablation of the labeled EC, ablations were carried out on the tip of EC membranes to ensure consistency of ablations from cell to cell and maximize the distance between the site of ablation and the nucleus as nuclear ablation invariably leads to cell death. For all experiments that utilize mosaic fluorescent membrane GFP labeling, all labeled single cells across the large palmoplantar surface of the mouse paw were longitudinally tracked manually. Briefly, to induce single-cell labeling of ECs, neonatal *VECadherinCreER; mTmG* pups received a single low dose of tamoxifen (2μg) at P2, allowing for sporadic single EC recombination throughout the vascular plexus. To ensure a sufficient number of ECs is available for manual segmentation and quantification of migration in relation to conserved vascular structures, we acquired large mosaics of the palmoplantar surface with

a minimum of 3×5 tiles of 444μm × 444μm area per tile across all revisits. ECs were manually tracked across time points (2-day revisits) and selected for analysis as long as they were present in the skin capillary plexus and could be resolved across all time points for displacement quantification.

Image analysis: Raw image stacks were imported for analysis into FIJI (ImageJ v1.52p, NIH) or Imaris software (v.9.5.1; Bitplane/Oxford Instruments). Individual optical planes, summed or max Z stacks of sequential optical sections were used to assemble figures. The tiled images were stitched by a grid/collection stitching plugin in Fiji. Prism software (Graphpad, v.8.0.0) was used to graph the data. EC migration (average normalized displacement) was determined based on the schematic and calculations depicted in Figure S3A. Briefly, we measured and averaged trailing- and leading-edge membrane displacements between successive time points to assess average displacement. This value was then normalized to the expansion factor of the occupied vessel to correct for vessel growth, resulting in the average normalized displacement value. Pearson's correlation coefficients were calculated using ImageJ software.

Whole-mount immunostaining: Mouse hind paw tissues were processed for whole-mount staining. Briefly, full-thickness paw skin was dissected and fixed in 4% paraformaldehyde (PFA) in PBS for 4–6 hours at room temperature, washed in PBS, and then blocked with 0.2% Triton X-100, 5% normal donkey serum, 1 % BSA in PBS overnight at 37°C. The samples were then incubated with primary antibodies for 48–72 h and secondary antibodies for 24 h on a rocker at 37°C. The anti-phospho-histone H3 (Ser10) antibody was from EMD Millipore (06–570) and was used at a 1:100-fold dilution; anti-Flk-1 (VEGFR2) antibody was from BD Biosciences (555307) and was used at 1:100-fold dilution; anti-ERG antibody was from Abcam (AB92513) and was used at 1:200-fold dilution; goat anti-rabbit IgG H&L (Alexa Fluor®) 568, goat anti-rat IgG H&L (Alexa Fluor®) 568, goat anti-Chicken IgY H&L (Alexa Fluor®) 488, and goat anti-rat IgG H&L (Alexa Fluor®) 488 was from ThermoFisher and was used at a 1:400-fold dilution. Tissue samples were mounted with Vectashield anti-fade mounting medium (Vector Laboratories) on individual slides and imaged on a LaVision TriM Scope II, as described in 'In vivo imaging.'

EdU incorporation assays: 5-Ethynyl-2′-deoxyuridine (EdU) was administered via intra-peritoneal injection (50 mg/kg in PBS) at indicated time-points before collecting tissue. Tissues were harvested and fixed in 4% paraformaldehyde (PFA) in PBS for 4–6 hours at room temperature, washed in PBS, and then blocked with 0.2% Triton X-100, 5% normal donkey serum, 1 % BSA in PBS overnight at 37°C. Anti-GFP antibody from Abcam (AB13970) was used at a 1:100-fold dilution to detect nuclear H2B-GFP signal (48 h at 37°C) prior to beginning the EdU labelling protocol. EdU labelling was performing using the Click-iT AlexaFluor 568 kit (Thermo Fisher) according to the manufacturer's instructions. Fixed whole-mount tissue was mounted on a slide with Vectashield anti-fade mounting medium (Vector Laboratories) and imaged on a LaVision TriM Scope II, as described in 'In vivo imaging.'

Pimonidazole-HCl labeling: Pimonidazole-HCl used to assess hypoxic status was from Hypoxyprobe, Inc (HP2–100Kit). Pimonidazole-HCl was administered via intra-peritoneal (60mg/kg in PBS) 90 minutes prior to tissue collection. Tissues were fixed in 4% paraformaldehyde (PFA) in PBS for 4–6 hours at room temperature, washed in PBS, and then blocked with 0.2% Triton X-100, 5% normal donkey serum, 1 % BSA in PBS overnight at 37°C. Tissues were stained with FITC-conjugated mouse monoclonal antibody to pimonidazole adducts (48 h at 37°C). and imaged on a LaVision TriM Scope II, as described in 'In vivo imaging.'

Flow cytometry: P5 and P21 *VECadCreER; mTmG* mice were euthanized for fluorescence activated cell sorting (FACS) 3-days post tamoxifen induction (P2, 100 μg intragastric; P18, 2 mg intraperitoneal). Dermal single cell suspensions were prepared for flow cytometry with a protocol adapted from previously described[55]. Briefly, back skin was incubated for 1 hour at 37 °C in 0.3 % trypsin (Sigma-Aldrich) in 150 mM NaCl, 0.5 mM KCl and 0.5 mM glucose. The dermis was physically separated from the epidermis, minced, and incubated in 2 mLs of collagenase (Sigma; C2674–11MG) at 125 U/mL final concentration in Hank's Balanced Salt Solution (HBSS; Gibco 14170–112) with no calcium, magnesium chloride, or magnesium sulfate for 2 hours at 37°C. The resulting cells were crushed and filtered through a 70 μm filter and spun at 240G for 10 minutes. All samples were pre-treated with rat serum (Sigma-Aldrich), and incubated with anti-mouse/human CD309 (Flk-1/VEGFR2)-APC (Thermofisher, 17-5821-81; 1:100) for 30 minutes at 4°C. Samples were run on a Becton Dickinson LSRII outfitted with Diva software v 8.0.1, and the data was analyzed using Flowjo v10.6.2.

VEGF-A Quantikine ELISA & skin sample preparation: Paw skin was excised, flash frozen with liquid nitrogen and stored at −80°C until all samples were collected. The tissue was then processed for lysate using a standard western blot protocol. In short, samples were homogenized with 100 μls of RIPA buffer (Sigma-Aldrich; R0278) containing a phosphatase inhibitor (Sigma; 4906845001) and protease inhibitor (Sigma; 11697498001), incubated on ice for 30 minutes, and then spun at 15,000G for 10 minutes. Supernatants were then transferred to a clean 1.5 ml Eppendorf and stored at −80°C.

Full thickness paw tissue lysate concentration from either P6, P15 or adult mice (2 months) were first quantified using a Pierce BCA Protein Assay Kit (Thermofisher; 23225) with absorbance read using a Glomax Explorer Microplate reader (Promega) at 560 nm and normalized for amount of total protein across all samples. The levels of mouse VEGF-A in paw lysates were then analyzed using a Quantikine ELISA kit specific for VEGF-A$_{164}$ and VEGF-A$_{120}$ (R&D Systems; MMV00) according to the manufacturer's protocol and absorbance was read using a Glomax Explorer Microplate Reader at 450 nm.

Quantification and Statistical Analysis: Statistical calculations were performed using Prism software (GraphPad, v.8.0.0). A two-sided unpaired t-test was used to determine the statistical significance between two experimental conditions. One-way ANOVA followed by Tukey's multiple comparisons test was utilized for multiple comparisons. A p-value of <0.05 was considered significant; specific p-values are noted in the figure legends. No statistical method was used to predetermine sample size (n). Mouse numbers represent the biological

replicates; sample size and replicates are indicated in the figure legends. All experiments were conducted at least three times.

Supplementary Material

Refer to Web version on PubMed Central for supplementary material.

ACKNOWLEDGMENTS

REFERENCES

1. Augustin HG, and Koh GY (2017). Organotypic vasculature: From descriptive heterogeneity to functional pathophysiology. Science 357. 10.1126/science.aal2379.

2. Swift MR, and Weinstein BM (2009). Arterial-venous specification during development. Circ Res 104, 576–588. 10.1161/circresaha.108.188805. [PubMed: 19286613]

3. Rocha SF, and Adams RH (2009). Molecular differentiation and specialization of vascular beds. Angiogenesis 12, 139–147. 10.1007/s10456-009-9132-x. [PubMed: 19212819]

4. Ellis CG, Jagger J, and Sharpe M (2005). The microcirculation as a functional system. Crit Care 9 Suppl 4, S3–8. 10.1186/cc3751. [PubMed: 16168072]

5. Herbert SP, and Stainier DY (2011). Molecular control of endothelial cell behaviour during blood vessel morphogenesis. Nat Rev Mol Cell Biol 12, 551–564. 10.1038/nrm3176. [PubMed: 21860391]

6. Bautch VL, and Caron KM (2015). Blood and lymphatic vessel formation. Cold Spring Harb Perspect Biol 7, a008268. 10.1101/cshperspect.a008268. [PubMed: 25731762]

7. Udan RS, Vadakkan TJ, and Dickinson ME (2013). Dynamic responses of endothelial cells to changes in blood flow during vascular remodeling of the mouse yolk sac. Development 140, 4041–4050. 10.1242/dev.096255. [PubMed: 24004946]

8. McDonald AI, Shirali AS, Aragón R, Ma F, Hernandez G, Vaughn DA, Mack JJ, Lim TY, Sunshine H, Zhao P, et al. (2018). Endothelial Regeneration of Large Vessels Is a Biphasic Process Driven by Local Cells with Distinct Proliferative Capacities. Cell Stem Cell 23, 210–225 e216. 10.1016/j.stem.2018.07.011. [PubMed: 30075129]

9. Chong DC, Yu Z, Brighton HE, Bear JE, and Bautch VL (2017). Tortuous Microvessels Contribute to Wound Healing via Sprouting Angiogenesis. Arterioscler Thromb Vasc Biol 37, 1903–1912. 10.1161/atvbaha.117.309993. [PubMed: 28838921]

10. Park H, Furtado J, Poulet M, Chung M, Yun S, Lee S, Sessa WC, Franco CA, Schwartz MA, and Eichmann A (2021). Defective Flow-Migration Coupling Causes Arteriovenous Malformations in Hereditary Hemorrhagic Telangiectasia. Circulation 144, 805–822. 10.1161/circulationaha.120.053047. [PubMed: 34182767]

11. Dekoninck S, Hannezo E, Sifrim A, Miroshnikova YA, Aragona M, Malfait M, Gargouri S, de Neunheuser C, Dubois C, Voet T, et al. (2020). Defining the Design Principles of Skin Epidermis Postnatal Growth. Cell 181, 604–620 e622. 10.1016/j.cell.2020.03.015. [PubMed: 32259486]

12. Coelho-Santos V, Berthiaume AA, Ornelas S, Stuhlmann H, and Shih AY (2021). Imaging the construction of capillary networks in the neonatal mouse brain. Proc Natl Acad Sci U S A 118. 10.1073/pnas.2100866118.

13. Takeo M, Chou WC, Sun Q, Lee W, Rabbani P, Loomis C, Taketo MM, and Ito M (2013). Wnt activation in nail epithelium couples nail growth to digit regeneration. Nature 499, 228–232. 10.1038/nature12214. [PubMed: 23760480]

14. Gore AV, Monzo K, Cha YR, Pan W, and Weinstein BM (2012). Vascular development in the zebrafish. Cold Spring Harb Perspect Med 2, a006684. 10.1101/cshperspect.a006684. [PubMed: 22553495]

15. Udan RS, Culver JC, and Dickinson ME (2013). Understanding vascular development. Wiley Interdiscip Rev Dev Biol 2, 327–346. 10.1002/wdev.91. [PubMed: 23799579]

16. Tsuruta D, Green KJ, Getsios S, and Jones JC (2002). The barrier function of skin: how to keep a tight lid on water loss. Trends Cell Biol 12, 355–357. 10.1016/s0962-8924(02)02316-4. [PubMed: 12191905]

17. Yokouchi M, Atsugi T, Logtestijn MV, Tanaka RJ, Kajimura M, Suematsu M, Furuse M, Amagai M, and Kubo A (2016). Epidermal cell turnover across tight junctions based on Kelvin's tetrakaidecahedron cell shape. Elife 5. 10.7554/eLife.19593.

18. Charkoudian N (2003). Skin blood flow in adult human thermoregulation: how it works, when it does not, and why. Mayo Clin Proc 78, 603–612. 10.4065/78.5.603. [PubMed: 12744548]

19. Kupper TS, and Fuhlbrigge RC (2004). Immune surveillance in the skin: mechanisms and clinical consequences. Nat Rev Immunol 4, 211–222. 10.1038/nri1310. [PubMed: 15039758]

20. Li KN, Jain P, He CH, Eun FC, Kang S, and Tumbar T (2019). Skin vasculature and hair follicle cross-talking associated with stem cell activation and tissue homeostasis. Elife 8. 10.7554/eLife.45977.

21. Pineda CM, Park S, Mesa KR, Wolfel M, Gonzalez DG, Haberman AM, Rompolas P, and Greco V (2015). Intravital imaging of hair follicle regeneration in the mouse. Nat Protoc 10, 1116–1130. 10.1038/nprot.2015.070. [PubMed: 26110716]

22. Marsh E, Gonzalez DG, Lathrop EA, Boucher J, and Greco V (2018). Positional Stability and Membrane Occupancy Define Skin Fibroblast Homeostasis In Vivo. Cell 175, 1620–1633 e1613. 10.1016/j.cell.2018.10.013. [PubMed: 30415836]

23. Kamberov YG, Karlsson EK, Kamberova GL, Lieberman DE, Sabeti PC, Morgan BA, and Tabin CJ (2015). A genetic basis of variation in eccrine sweat gland and hair follicle density. Proc Natl Acad Sci U S A 112, 9932–9937. 10.1073/pnas.1511680112. [PubMed: 26195765]

24. Sörensen I, Adams RH, and Gossler A (2009). DLL1-mediated Notch activation regulates endothelial identity in mouse fetal arteries. Blood 113, 5680–5688. 10.1182/blood-2008-08-174508. [PubMed: 19144989]

25. Muzumdar MD, Tasic B, Miyamichi K, Li L, and Luo L (2007). A global double-fluorescent Cre reporter mouse. Genesis 45, 593–605. 10.1002/dvg.20335. [PubMed: 17868096]

26. Franco CA, Jones ML, Bernabeu MO, Geudens I, Mathivet T, Rosa A, Lopes FM, Lima AP, Ragab A, Collins RT, et al. (2015). Dynamic endothelial cell rearrangements drive developmental vessel regression. PLoS Biol 13, e1002125. 10.1371/journal.pbio.1002125. [PubMed: 25884288]

27. Abraham S, Scarcia M, Bagshaw RD, McMahon K, Grant G, Harvey T, Yeo M, Esteves FOG, Thygesen HH, Jones PF, et al. (2015). A Rac/Cdc42 exchange factor complex promotes formation of lateral filopodia and blood vessel lumen morphogenesis. Nat Commun 6, 7286. 10.1038/ncomms8286. [PubMed: 26129894]

28. Chen Q, Jiang L, Li C, Hu D, Bu JW, Cai D, and Du JL (2012). Haemodynamics-driven developmental pruning of brain vasculature in zebrafish. PLoS Biol 10, e1001374. 10.1371/journal.pbio.1001374. [PubMed: 22904685]

29. Kochhan E, Lenard A, Ellertsdottir E, Herwig L, Affolter M, Belting HG, and Siekmann AF (2013). Blood flow changes coincide with cellular rearrangements during blood vessel pruning in zebrafish embryos. PLoS One 8, e75060. 10.1371/journal.pone.0075060. [PubMed: 24146748]

30. Ahn SJ, Ruiz-Uribe NE, Li B, Porter J, Sakadzic S, and Schaffer CB (2020). Label-free assessment of hemodynamics in individual cortical brain vessels using third harmonic generation microscopy. Biomed Opt Express 11, 2665–2678. 10.1364/boe.385848. [PubMed: 32499951]

31. Lenard A, Daetwyler S, Betz C, Ellertsdottir E, Belting HG, Huisken J, and Affolter M (2015). Endothelial cell self-fusion during vascular pruning. PLoS Biol 13, e1002126. 10.1371/journal.pbio.1002126. [PubMed: 25884426]

32. Sun JF, Phung T, Shiojima I, Felske T, Upalakalin JN, Feng D, Kornaga T, Dor T, Dvorak AM, Walsh K, and Benjamin LE (2005). Microvascular patterning is controlled by fine-tuning the Akt signal. Proc Natl Acad Sci U S A 102, 128–133. 10.1073/pnas.0403198102. [PubMed: 15611473]

33. Tumbar T, Guasch G, Greco V, Blanpain C, Lowry WE, Rendl M, and Fuchs E (2004). Defining the epithelial stem cell niche in skin. Science 303, 359–363. 10.1126/science.1092436. [PubMed: 14671312]

34. Chang AH, Raftrey BC, D'Amato G, Surya VN, Poduri A, Chen HI, Goldstone AB, Woo J, Fuller GG, Dunn AR, and Red-Horse K (2017). DACH1 stimulates shear stress-guided endothelial cell migration and coronary artery growth through the CXCL12-CXCR4 signaling axis. Genes Dev 31, 1308–1324. 10.1101/gad.301549.117. [PubMed: 28779009]

35. Mesa KR, Rompolas P, Zito G, Myung P, Sun TY, Brown S, Gonzalez DG, Blagoev KB, Haberman AM, and Greco V (2015). Niche-induced cell death and epithelial phagocytosis regulate hair follicle stem cell pool. Nature 522, 94–97. 10.1038/nature14306. [PubMed: 25849774]

36. Voehringer D, Liang HE, and Locksley RM (2008). Homeostasis and effector function of lymphopenia-induced "memory-like" T cells in constitutively T cell-depleted mice. J Immunol 180, 4742–4753. 10.4049/jimmunol.180.7.4742. [PubMed: 18354198]

37. Jeong HW, Hernández-Rodríguez B, Kim J, Kim KP, Enriquez-Gasca R, Yoon J, Adams S, Schöler HR, Vaquerizas JM, and Adams RH (2017). Transcriptional regulation of endothelial cell behavior during sprouting angiogenesis. Nat Commun 8, 726. 10.1038/s41467-017-00738-7. [PubMed: 28959057]

38. Wakabayashi T, Naito H, Suehiro JI, Lin Y, Kawaji H, Iba T, Kouno T, Ishikawa-Kato S, Furuno M, Takara K, et al. (2018). CD157 Marks Tissue-Resident Endothelial Stem Cells with Homeostatic and Regenerative Properties. Cell Stem Cell 22, 384–397 e386. 10.1016/j.stem.2018.01.010. [PubMed: 29429943]

39. Lohela M, Bry M, Tammela T, and Alitalo K (2009). VEGFs and receptors involved in angiogenesis versus lymphangiogenesis. Curr Opin Cell Biol 21, 154–165. 10.1016/j.ceb.2008.12.012. [PubMed: 19230644]

40. Prewett M, Huber J, Li Y, Santiago A, O'Connor W, King K, Overholser J, Hooper A, Pytowski B, Witte L, et al. (1999). Antivascular endothelial growth factor receptor (fetal liver kinase 1) monoclonal antibody inhibits tumor angiogenesis and growth of several mouse and human tumors. Cancer Res 59, 5209–5218. [PubMed: 10537299]

41. Witte L, Hicklin DJ, Zhu Z, Pytowski B, Kotanides H, Rockwell P, and Böhlen P (1998). Monoclonal antibodies targeting the VEGF receptor-2 (Flk1/KDR) as an anti-angiogenic therapeutic strategy. Cancer Metastasis Rev 17, 155–161. 10.1023/a:1006094117427. [PubMed: 9770111]

42. Karaman S, Paavonsalo S, Heinolainen K, Lackman MH, Ranta A, Hemanthakumar KA, Kubota Y, and Alitalo K (2022). Interplay of vascular endothelial growth factor receptors in organ-specific vessel maintenance. J Exp Med 219. 10.1084/jem.20210565.

43. Han HC (2012). Twisted blood vessels: symptoms, etiology and biomechanical mechanisms. J Vasc Res 49, 185–197. 10.1159/000335123. [PubMed: 22433458]

44. Owen CG, Newsom RS, Rudnicka AR, Barman SA, Woodward EG, and Ellis TJ (2008). Diabetes and the tortuosity of vessels of the bulbar conjunctiva. Ophthalmology 115, e27–32. 10.1016/j.ophtha.2008.02.009. [PubMed: 18423868]

45. Nagy JA, Chang SH, Dvorak AM, and Dvorak HF (2009). Why are tumour blood vessels abnormal and why is it important to know? Br J Cancer 100, 865–869. 10.1038/sj.bjc.6604929. [PubMed: 19240721]

46. Korn C, and Augustin HG (2015). Mechanisms of Vessel Pruning and Regression. Dev Cell 34, 5–17. 10.1016/j.devcel.2015.06.004. [PubMed: 26151903]

47. Ehling M, Adams S, Benedito R, and Adams RH (2013). Notch controls retinal blood vessel maturation and quiescence. Development 140, 3051–3061. 10.1242/dev.093351. [PubMed: 23785053]

48. Andrade J, Shi C, Costa ASH, Choi J, Kim J, Doddaballapur A, Sugino T, Ong YT, Castro M, Zimmermann B, et al. (2021). Control of endothelial quiescence by FOXO-regulated metabolites. Nat Cell Biol 23, 413–423. 10.1038/s41556-021-00637-6. [PubMed: 33795871]

49. Trojanowska M (2010). Cellular and molecular aspects of vascular dysfunction in systemic sclerosis. Nat Rev Rheumatol 6, 453–460. 10.1038/nrrheum.2010.102. [PubMed: 20585340]

50. Antonios TF, Singer DR, Markandu ND, Mortimer PS, and MacGregor GA (1999). Structural skin capillary rarefaction in essential hypertension. Hypertension 33, 998–1001. 10.1161/01.hyp.33.4.998. [PubMed: 10205237]

51. Li L, Mac-Mary S, Sainthillier JM, Nouveau S, de Lacharriere O, and Humbert P (2006). Age-related changes of the cutaneous microcirculation in vivo. Gerontology 52, 142–153. 10.1159/000091823. [PubMed: 16645294]

52. Demonbreun AR, Quattrocelli M, Barefield DY, Allen MV, Swanson KE, and McNally EM (2016). An actin-dependent annexin complex mediates plasma membrane repair in muscle. J Cell Biol 213, 705–718. 10.1083/jcb.201512022. [PubMed: 27298325]

53. Bansal D, Miyake K, Vogel SS, Groh S, Chen CC, Williamson R, McNeil PL, and Campbell KP (2003). Defective membrane repair in dysferlin-deficient muscular dystrophy. Nature 423, 168–172. 10.1038/nature01573. [PubMed: 12736685]

54. Martin JD, Seano G, and Jain RK (2019). Normalizing Function of Tumor Vessels: Progress, Opportunities, and Challenges. Annu Rev Physiol 81, 505–534. 10.1146/annurev-physiol-020518-114700. [PubMed: 30742782]

55. Mohammed J, Beura LK, Bobr A, Astry B, Chicoine B, Kashem SW, Welty NE, Igyártó BZ, Wijeyesinghe S, Thompson EA, et al. (2016). Stromal cells control the epithelial residence of DCs and memory T cells by regulated activation of TGF-β. Nat Immunol 17, 414–421. 10.1038/ni.3396. [PubMed: 26901152]

HIGHLIGHTS

- Plexus maturation is mediated by coordinated regression and rearrangement of ECs

- Adult ECs are positionally stable but reactivate migration following local ablation

- Global ablation reveals resilience of network architecture to large-scale cell loss

- Adult but not neonatal ECs are competent for plasmalemmal self-repair

INCLUSION AND DIVERSITY

We support the inclusive, diverse, and equitable conduct of research.
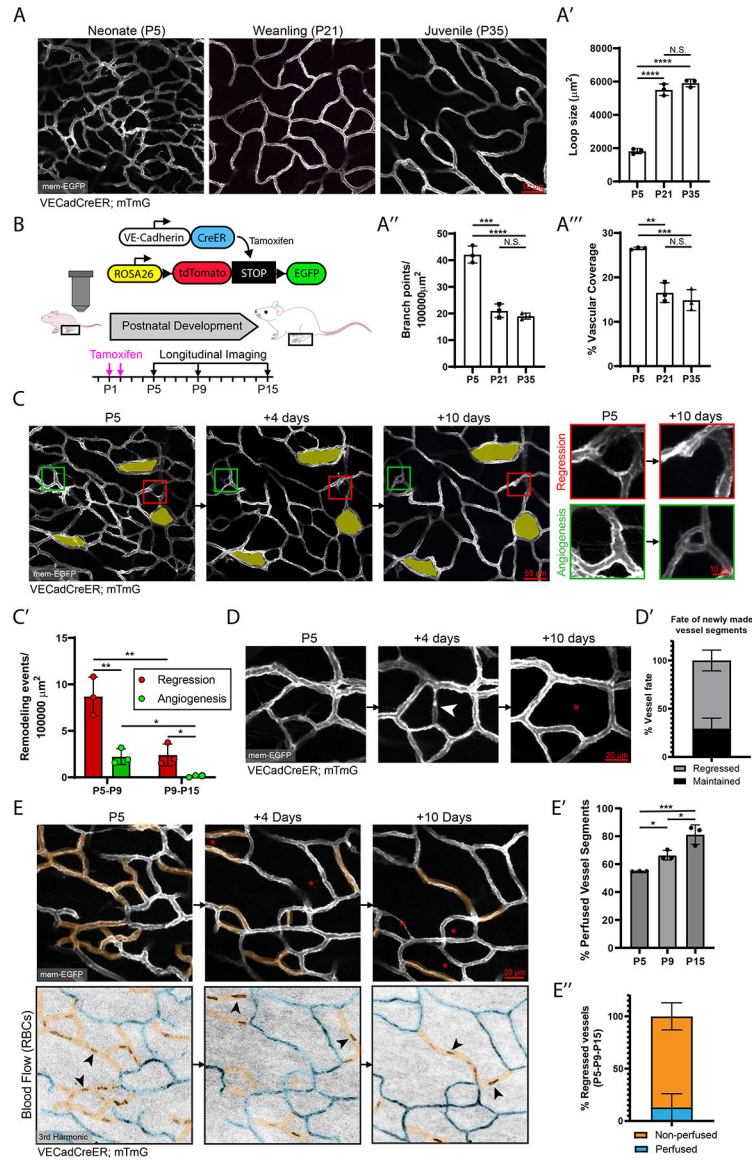
Figure 1. Vessel regression drives maturation of the capillary network to optimize network perfusion.

(A) Static comparison of the capillary plexus of P5, P21, and P35 skin of *VECadCreER; mTmG* mice. (A', A" & A'") Quantification of capillary loop size (μm^2), branching points, and % vascular coverage (n=3 mice). **, P<0.01; ***, P<0.001; ****, P<0.0001 by one-way ANOVA followed by Tukey's MCT. (B) Schematic of the *VECadCreER; mTmG* reporter and longitudinal imaging workflow. (C) Longitudinal tracking of the capillary plexus at P5, P9 and P15. The same loops are pseudocolored in yellow. Example of regression (red inset) and angiogenesis events (Green inset). (C') Quantification of overall vessel remodeling from P5-P9 and P9-P15 (n=3 mice). *, P<0.05; **, P<0.01 by unpaired Student's t-test. (D) Tracking of vessels angiogenesis (white arrowhead) at P5-P9 revisited at P15. (D') Quantification of the fate of angiogenesis events during P5-P9 revisited at P15 (n=38 events from 3 mice). (E) Tracking of vessel remodeling (top panel) and network perfusion (bottom panel) at P5, P9, and P15. Perfused segments are pseudocolored blue;

non-perfused segments are pseudocolored orange. Red asterisks denote regressed segments. Black arrowheads show examples of stalled RBCs. (E') Quantification of the percentage of perfused vessels at P5, P9, and P15 (n=3 mice). *, P<0.05; ***, P<0.001; ****, by one-way ANOVA followed by Tukey's MCT. (E") Quantification of perfusion status of regressed vessels tracked from P5-P9-P15 (n=80 events from 3 mice). For all bar graphs error bars are mean ± standard deviation.
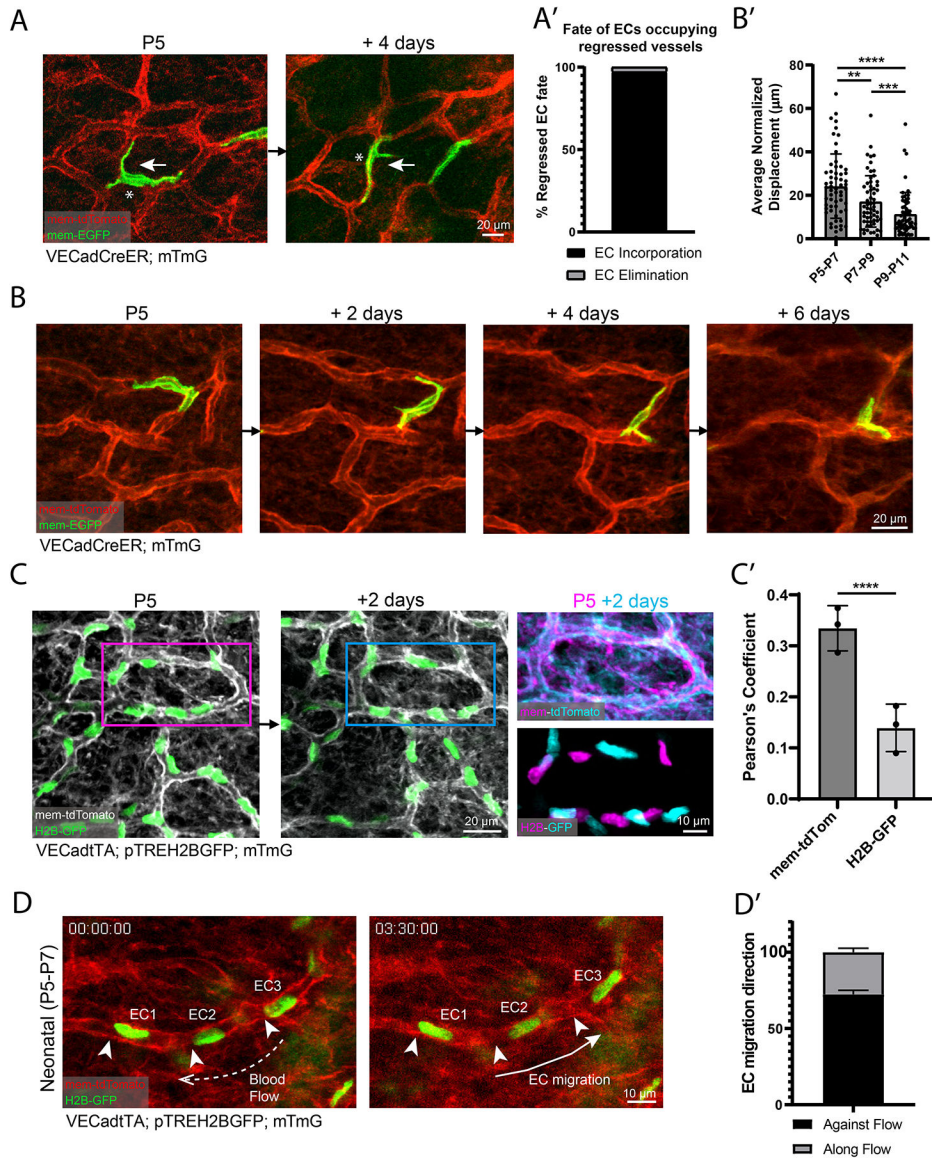
Figure 2. Neonatal ECs participate in plexus-wide positional rearrangement and execute vessel regression via migration.

(A) Tracking of single ECs undergoing vessel regression (white asterisk). White arrow depicts migration direction. (A') Quantification of regressed EC fate (n=38 cells from 5 mice). (B) 2-day revisits of an EC migrating within existing vessel architecture. (B') Quantification of EC migration in 2-day intervals from P5-P11(n=60 cells from 3 mice). **, $P<0.01$; ***, $P<0.001$; ****, $P<0.0001$ by one-way ANOVA followed by Tukey's post-hoc test. (C) P5 to P7 revisit of EC nuclear reporter (*VECadtTA; pTREH2BGFP; mTmG*). Overlay of P5 EC positions (magenta) compared to P7(cyan) indicates EC positional change. (C') Quantification of the Pearson's correlation coefficient between membrane signal compared to nuclear signal of P5 vs P7 vessels (n=3 mice). ****, $P<0.0001$ by unpaired Student's t-test. (D) Time-lapse imaging of EC nuclei (numbered) migration in neonatal vessels. White arrowheads indicate initial EC positions, dotted arrow denotes direction of blood flow, and solid arrow indicates EC migration direction. (D')

Quantification of EC migration polarization direction (n=86 ECs from 3 mice). For all bar graphs error bars are mean ± standard deviation.
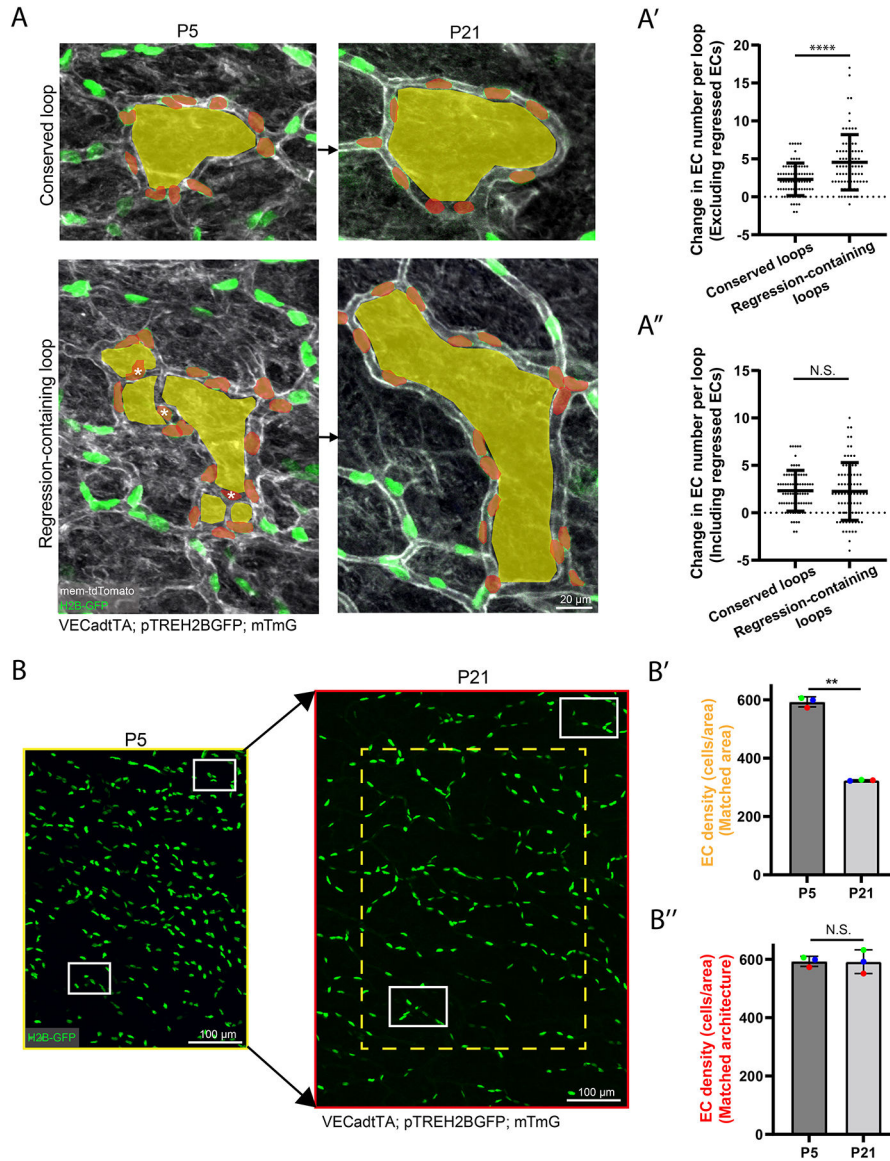
Figure 3. Cellular density in the developing plexus is locally controlled by the incorporation of ECs from regressed segments.

(A) Comparison of changes in EC number in conserved and regression-containing loops tracked from P5 to P21 in *VECadtTA; pTREH2BGFP; mTmG* mice. Examples of conserved loops (top panel) and regression-containing loops (bottom panel) with pseudocolored loops (yellow) and nuclei within loops of interest (red). ECs within regressed vessels are marked with white asterisks. (A') Quantification of the change in EC number between conserved loops and regression-containing loops excluding regressed ECs (white asterisks) or (A") including regressed ECs (n=150 capillary loops from 3 mice). ****, P<0.0001 by unpaired Student's t-test. (B) Tracking of EC nuclei within the same vascular architecture in P5 and P21 mice. White boxes indicate matching regions of revisits. (B') Quantification of EC density normalized to area Yellow box indicates matched P5 area (250000 μm^2) in the P21 plexus (n=3 mice). (B") Quantification of EC density matched to conserved vessel architecture. Red outline indicates matched P5 architecture at P21 (460000 μm^2) (n=3 mice).

**, P<0.01 by unpaired Student's t-test. For all graphs error bars are mean ± standard deviation.
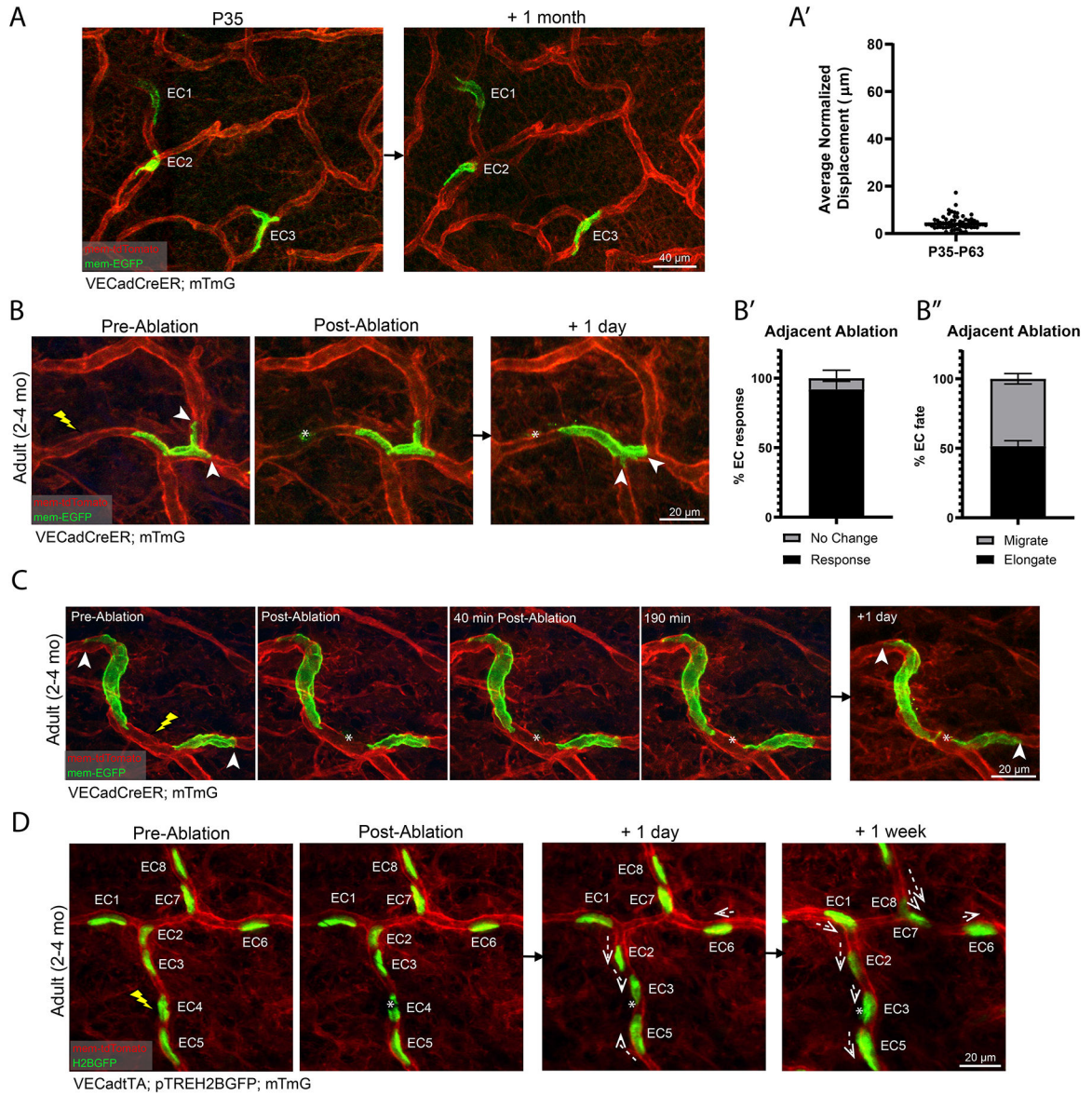
Figure 4. ECs become positionally stable in adulthood but coordinate neighborhood rearrangement in response to local ablation.

(A) Single ECs (numbered) in *VECadCreER; mTmG* mice at P35 longitudinally tracked over 1-month. (A') Quantification of EC migration from P35 to P63 (n=60 cells from 3 mice). (B) Adult vessel (2–4 months) inflicted with targeted laser ablation adjacent to single labeled ECs followed by 1-day revisit. (B') The vast majority (>90%) of all labeled cells respond to adjacent laser ablation. (B") ECs adjacent to an ablation respond by migrating or elongating with approximately equal probability (n=180 cells from 3 mice). (C) Time-lapse of a laser ablation targeted in between two labeled ECs followed by 24 h revisit. (D) Tracking of EC nuclei (numbered) inflicted with laser ablation followed by 24 h and 1 week revisits (n=3 mice). Dotted arrows indicate migration direction. For all images, lightning bolt denotes the sites targeted for ablation; white arrowheads denote sites of anchorage;

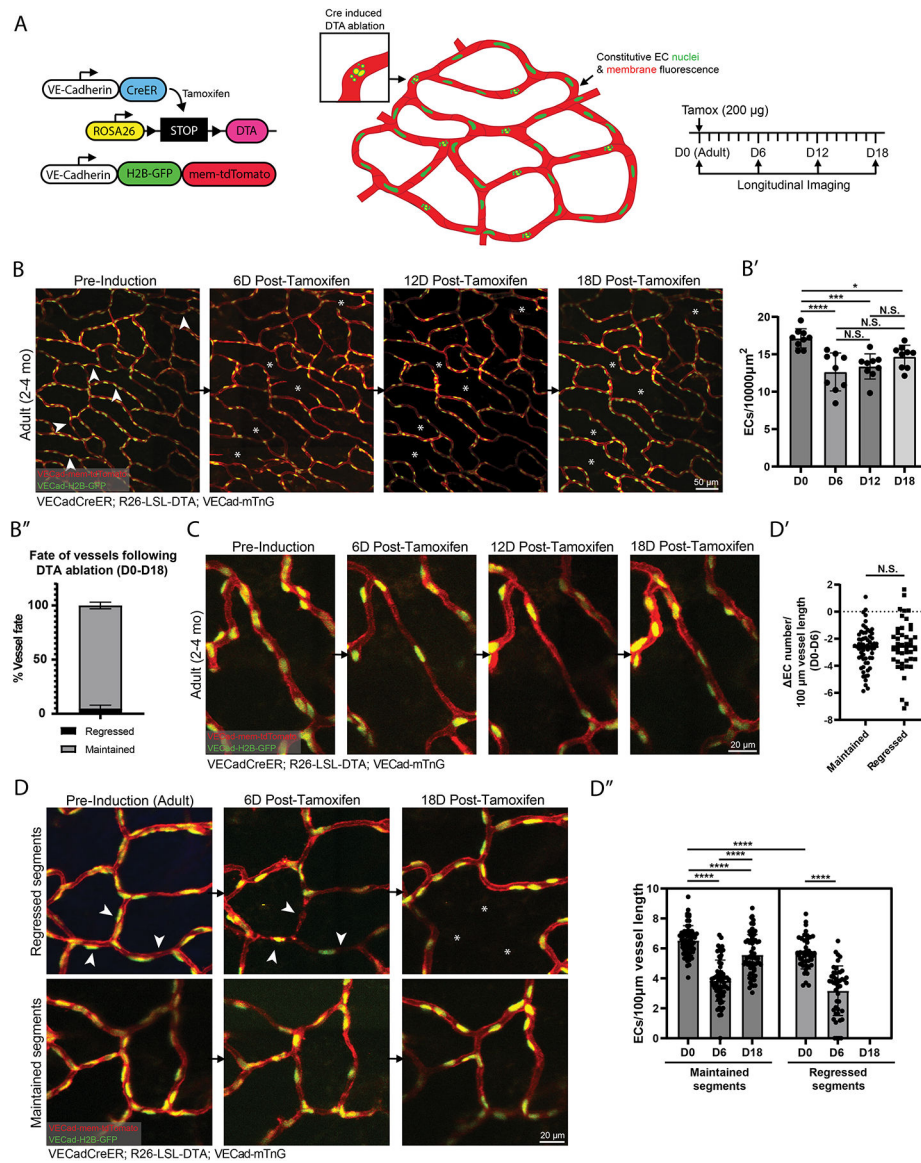white asterisks denote the ablated region. For all bar graphs error bars are mean ± standard deviation.

Figure 5. Network-wide ablation of adult ECs reveals the coordinated maintenance of plexus architecture by surviving ECs.

(A) Schematic of the *VECadCreER; R26-LSL-DTA; VECad-mTnG* model and imaging workflow. (B) Tracking of EC network at pre-induction, 6-, 12-, and 18-days post-tamoxifen induction. (B') Quantification of EC density tracked at pre-induction, 6-, 12-, and 18-days post-tamoxifen induction (n=3 mice). **, P<0.01; ***, P<0.001; ****, P<0.0001 by one-way ANOVA followed by Tukey's MCT. (B") Quantification of vessel fate from pre-induction to 18-days post-tamoxifen (n= 830 vessels from 3 mice). (C) Example of vessel recovery following DTA ablation. (D) (Top panel) Vessel segments that underwent regression at pre-induction, 6-, and 18-days post tamoxifen induction. (Bottom panel) Vessel segments that were maintained at the corresponding time-points. (D') Quantification of the change in EC number per 100 µm vessel length within maintained versus regressed segments from pre-induction to 6-days post-tamoxifen induction. N.S, not significant by unpaired Student's t-test. (D") Quantification of EC number per 100 µm vessel length

within maintained versus regressed vessel segments from pre-induction, 6-, and 18-days post-tamoxifen induction (n=63 maintained and 44 regressed vessels from 3 mice). P<0.001; ****, by one-way ANOVA followed by Tukey's MCT for maintained segments. ****, P<0.0001 by unpaired Student's t-test for regressed segments (pre-induction vs 6-days post-tamoxifen) and maintained vs regressed segments (pre-induction). For all images, white arrowheads indicate vessels fated for regression and white asterisks denote the location of vessels that were regressed. For all graphs error bars are mean ± standard deviation.
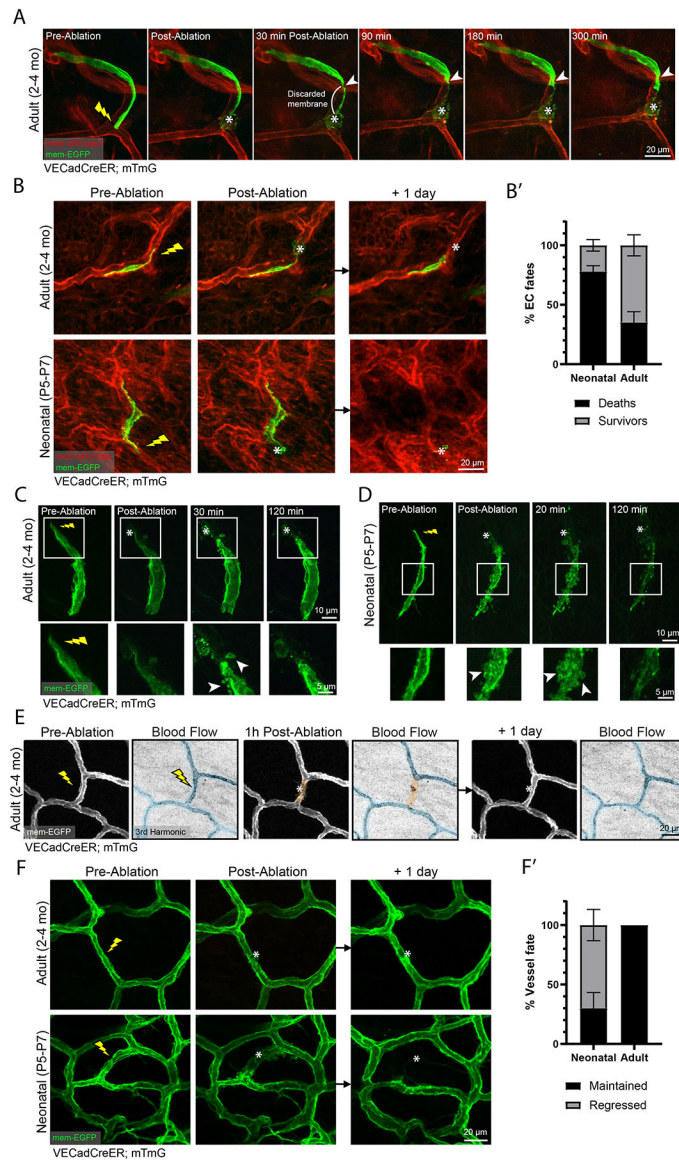
Figure 6. Adult but not neonatal ECs preferentially activate a plasmalemmal self-repair mechanism to survive injury and preserve the vascular architecture.

(A) Time-lapse of a labeled EC (*VECadCreER; mTmG*) inflicted with laser damage. White arrowhead denotes site of excision (n=4 mice). (B) (Top panel) Adult EC induced with laser ablation followed by 1-day revisit. (Bottom panel) A neonatal EC inflicted with laser ablation followed by 1-day revisit. (B') Quantification of neonatal versus adult EC fates 1-day post laser ablation (n=60 neonatal cells; n=84 adult cells from 3 mice respectively). (C) Time-lapse of a labeled adult EC inflicted with laser ablation (inset; white arrowheads denote localized membrane blebs) (n=3 mice). (D) Time-lapse of a labeled neonatal EC inflicted with laser ablation (inset; white arrowheads denote membrane blebbing) (n=3 mice). (E) Tracking of blood flow status of an adult vessel 1-hour and 1-day post-laser ablation. Perfused segments are pseudocolored blue; non-perfused segments are pseudocolored orange (n=3 mice). (F) Tracking of adult (top panel) and neonatal (bottom panel) vessel fate 1-day post ablation. (F') Quantification of vessel fates 1-day post-ablation

(n=88 neonatal vessels; n=99 adult vessels from 3 mice respectively). For all images, lightning bolt denotes the site of laser ablation; white asterisks denote the ablation site. For all bar graphs error bars are mean ± standard deviation.
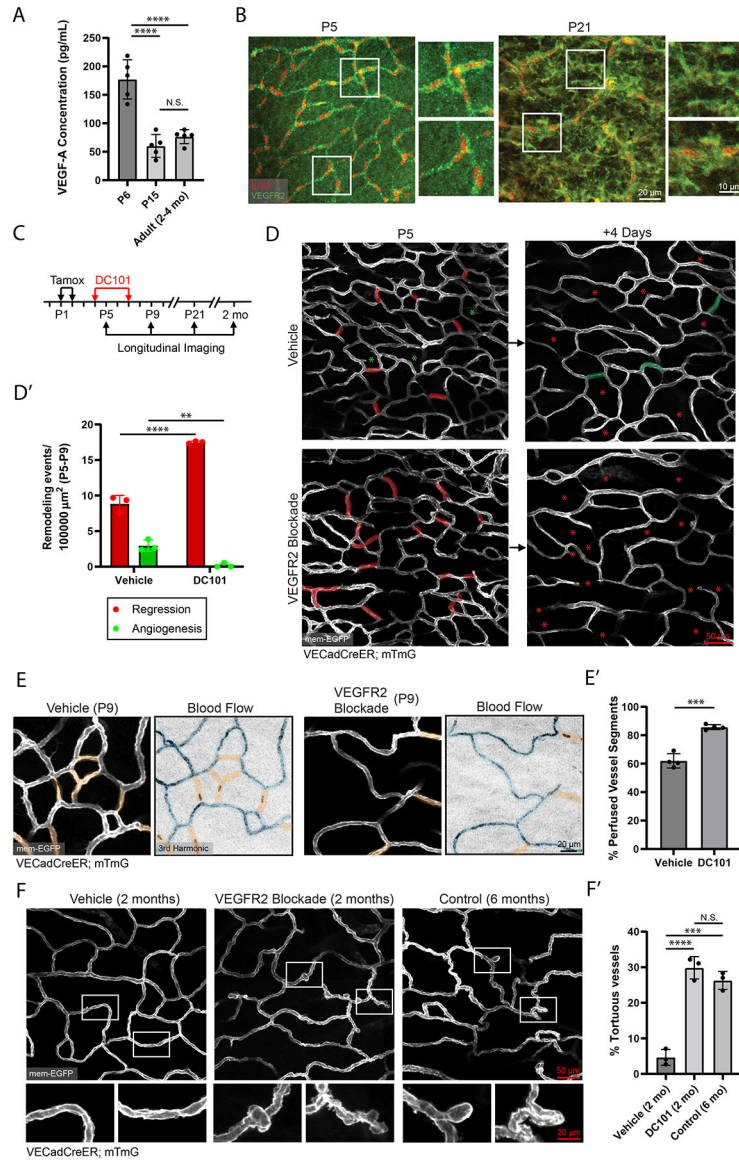
Figure 7. Neonatal vessel regression, optimization of network perfusion, and adult maintenance are orchestrated by neonatal VEGFR2 signaling.

(A) VEGF-A ELISA carried out on samples generated from P6, P15 and adult mouse paw skin (n=5 mice per condition). ****, P<0.0001 by one-way ANOVA followed by Tukey's MCT. (B) Whole-mount immunostaining of VEGFR2 (green) and ERG (red) in P5 and P21 mouse skin. (C) Schematic of DC101 administration and longitudinal imaging workflow. (D) Longitudinal imaging of vehicle (PBS) versus DC101 treated mice from P5 to P9. Regressed vessels are pseudocolored in red at P5 and red asterisks at P9. New vessels from angiogenesis are pseudocolored in green at P9 with green asterisks at P5. (D') Quantification of P5-P9 vessel remodeling in vehicle versus DC101 treated mice (n=3 mice). **, P<0.01; ****, P<0.0001 by unpaired Student's t-test. (E) Comparison of network perfusion between vehicle and DC101 treated animals at P9. Perfused segments are pseudocolored blue; non-perfused segments are pseudocolored orange. (E') Quantification of the percentage of perfused vessels in vehicle versus DC101 treated animals (n=470

vessels from vehicle and 341 vessels from DC101 treated animals across 4 mice). ***,
P<0.001 by unpaired Student's t-test. (F) Comparison of the vascular plexus of 2-month old
vehicle-, 2-month old DC101-treated, and 6-month old control mice. (F') Quantification of
the percentage of vessels exhibiting tortuous morphology in 2-month old vehicle-, 2-month
old DC101-treated and 6-month old control mice (n=3 mice). ***, P<0.001; ****, P<0.0001
by one-way ANOVA followed by Tukey's MCT. For all bar graphs error bars are mean ±
standard deviation.

KEY RESOURCES TABLE

REAGENT or RESOURCE	SOURCE	IDENTIFIER
Antibodies		
Anti-phospho-Histone H3 (Ser10) Antibody	EMD Millipore	Cat#06–570 (RRID:AB_310177)
Rat Anti-Mouse Flk-1 Antibody (VEGFR2)	BD Pharmingen	Cat#555307 (RRID:AB_395720)
Anti-ERG Antibody [EPR3864]	Abcam	Cat#ab92513 (RRID:AB_2630401)
Anti-GFP Antibody	Abcam	Cat#ab13970 (RRID:AB_300798)
CD309 (Flk1) Antibody (Avas12a1), APC	ThermoFisher	Cat#17–5821-81 (RRID:AB_657866)
InVivoMab anti-mouse VEGFR2 (DC101)	BioXCell	Cat#BE0060 (RRID:AB_1107766)
Goat anti-Rabbit Alexa Fluor 568	ThermoFisher	Cat#A-11011 (RRID:AB_143157)
Goat anti-Rat Alexa Fluor 568	ThermoFisher	Cat#A-11077 (RRID:AB_2534121)
Goat anti-Rat Alexa Fluor 488	ThermoFisher	Cat#A-11006 (RRID:AB_2534074)
Goat anti-Chicken Alexa Fluor 488	ThermoFisher	Cat#11039 (RRID:AB_2534096)
Chemicals, Peptides, and Recombinant Proteins		
Tamoxifen	Sigma	Cat#T5648
EdU	ThermoFisher	Cat#A10044
Corn oil	Sigma	Cat#C8267–2.5L
Critical Commercial Assays		
Click-iT EdU Alexa-555 imaging Kit	Invitrogen	Cat#C10638
Hypoxyprobe Plus Kit (FITC-Mab)	Hypoxyprobe	Cat#HP2–100Kit
Mouse VEGF Quantikine ELISA Kit	R&D Systems	Cat#MMV00
Experimental Models: Organisms/Strains		
Cdh5(PAC) Cre-ERT2 (VECadherinCreER)	Laboratory of Ralf H. Adams	RRID:MGI:3848984
Rosa26-mT/mG	The Jackson Laboratory	RRID:IMSR_JAX:007576
VECadherin-tTA	The Jackson Laboratory	RRID:IMSR_JAX:013585
pTRE-H2BGFP	Laboratory of Elaine Fuchs	RRID:IMSR_JAX:005104
Rosa26-DTA (R26-LSL-DTA)	The Jackson Laboratory	RRID:IMSR_JAX:009669
Cdh5-mTnG (VECadherin-mTnG)	Laboratory of Ralf H. Adams	Jeong et al.[37]
CD1	Charles River	022
Software and Algorithms		
FIJI (ImageJ)	NIH	N/A
GraphPad Prism	GraphPad Software, inc	N/A
FlowJo	FLOWJO, LLC	N/A
Adobe Illustrator	Adobe	N/A
Adobe Photoshop	Adobe	N/A
Adobe Premier Pro	Adobe	N/A
Imaris	Bitplane/Oxford Instruments	N/A